JOURNAL OF SPACECRAFT AND ROCKETS
Vol. 31, No. 4, July–August 1994

Hypersonic Interceptor Aero-Optics Performance Predictions

George W. Sutton,* John E. Pond,† Ronald Snow,‡ and, Yanfang Hwang§
Aero Thermo Technology, Inc., Huntsville, Alabama 35806

This paper describes hypersonic interceptor aero-optics performance predictions. It includes code results for three-dimensional shapes and comparisons to initial experiments. It covers the aerothermal, aerodynamic computational codes that are capable of covering the entire flight regime from subsonic to hypersonic flow and includes chemical reactions and turbulence. Heat transfer to the various surfaces is calculated as an input to cooling and ablation processes. The aero-optics codes determine the effect of the mean flowfield and turbulence on the tracking and imaging capability of on-board optical sensors. This paper concentrates on the latter aspects.

Nomenclature

A = area, m^2
a = speed of sound, m/s
b = tip
C = correlation function
c = speed of light, m/s
D = aperture (lens) diameter
d = tilt
E_k = compressibility correction term
f = focus correction, m^{-1}
I = intensity at focal plane, w/cm^2
k = wave number $2\pi/\lambda$, m^{-1}
L = path length, m
ℓ' = turbulence scale length, m
M = Mach number
n = index of refraction
p = pressure, N/m^2
r = distance, m
T = temperature, K
t = time, s
U = velocity, m/s
u = scalar electric field, V/m
x, y, z = coordinates, m
β = Gladstone-Dale constant, m^3/g
ϵ = rate of turbulence dissipation, j/kg-s
ϵ, η = coordinates of ray pierce point of a CFD cell, m
ξ, η = orthogonal separation distances at the aperture
κ = turbulent kinetic energy, j/kg
λ = wavelength, m
ρ = density, kg/m^3; dimensionless distance between rays at the aperture
θ = angle from centerline of focal plane
σ = optical path length, m
τ = modulation transfer function
ζ = z dummy variable

Subscripts

2 = on surface of cone
A = aperture
c = coolant at exit
FF = flow field
i = ith species; nodes
o = initial
t = turbulent
T = turbulent
x = x-direction
y = y-direction
∞ = freestream

Superscripts

$\bar{}$ = mean
$'$ = fluctuation

Introduction

THE aero-optic effect is caused by changes in the index of refraction, which varies linearly with gas density for a single species and is proportional to partial densities for a mixture of different species. High gas density reduces light speed, and vice versa for low density. This retardation or acceleration causes the familiar refraction effects, such as total reflection from a hot road, but it also causes image distortion if the transverse gradient is not perfectly linear. The most familiar example of this is the curved mirror in a fun house. These effects in gases have been used to advantage for decades in optical diagnostics in wind tunnels, such as Schlieren, shadowgraphs, and interferometry.

If the gas is also turbulent with mixing of high- and low-density gases, the light wavefront distortion becomes random. The turbulent mixing then results in blurring, as well. The most familiar example of this is the enlargement of star images observed by ground-based telescopes due to atmospheric turbulence and objects when viewed through the exhaust of jet engines.

Similar effects occur to an optical sensor on a vehicle traveling through the atmosphere. The air far ahead of the vehicle is rather benign optically, but the flight vehicle transfers some of its kinetic energy into thermal and pressure energy of the air surrounding the vehicle, thereby changing its density. A typical example of this is a shockwave where the density behind the shockwave can be an order of magnitude higher than the ambient air ahead of the shockwave. At altitudes below about 40 km, the flow next to the vehicle optical window is usually turbulent. The turbulent boundary layer mixes air, which is at the temperature of the window, with the shock-heated air, which has a much higher temperature and therefore lower density. If wall jet cooling of the optical window is used, then cool coolant gas will be mixed with the hot shock layer gas.

These phenomena adversely affect the image quality of an optical sensor. The mean flowfield causes a boresight error and blurring and, if the flowfield is unsteady, jitter. The turbulence will cause blurring and very-high-frequency jitter. The blurring can cause a decrease in the signal-to-noise ratio and image

Presented as Paper 93-2675 at the 2nd AIAA/BMDO Interceptor Technology Conference, Albuquerque, NM, June 8–10, 1993; Received July 20, 1993; revision received Oct. 1, 1993; accepted for publication Oct. 5, 1993.

*Chief Scientist. Fellow AIAA.
†Senior Engineer. Member AIAA.
‡Senior Scientist.
§Engineer.

distortion, which adversely affects centroid location for precision tracking. By reciprocity, similar effects will occur to a laser beam emanating from the vehicle. This paper describes a new capability to evaluate these effects for any vehicle configuration and any coolant using physical optics (Fourier optics).

History

The first known analysis of turbulence aero-optics was performed by Liepmann.[1] He analyzed the random refraction (i.e., bending) of a single ray through a turbulent flow. His interpretation was that the rms deviation of the ray was the blur. We now know that this is the rms jitter of the centroid of the beam. Hufnagel performed an analysis using the modulation transfer function (MTF) of optics,[2] but his model of the turbulence was not physical.[3] Extensive measurements were made in the Ames supersonic wind tunnel of the blurring caused by a turbulent boundary layer.[4] The data were reduced by use of the Booker-Gordon small-scattering theory.[5] These results were interpreted by Sutton,[3] who deduced the relation of the optical turbulence parameters to the aerodynamic freestream density and Mach number. Sutton[6,7] also analyzed the optical blurring caused by turbulence and applied this to gas dynamic lasers[6] and aircraft.[7] Snow independently derived similar relations.[8] Wave optics approaches that are computer intensive have not been very successful. More recently, Sutton has extended his theory for turbulence to the case where the turbulence parameters also vary spatially in the flow direction.[9]

Summary

The simplest method for performing optical calculations is ray tracing. This uses the phenomenon of wave retardation to determine the change in direction (refraction) of a ray. Ray tracing is used extensively for lens and telescope design, but does not give rigorous results for either boresight error or the image blur circle. Ray tracing also does not predict wavelength effects correctly with regard to the magnitude of the blur circle. For example, for a diffraction-limited optical system, ray tracing predicts an infinitesimally small focal spot size independent of wavelength, instead of the diffractive point-spread function.

The second technique is physical optics, which predicts diffraction; that is, the interference effects between waves. To do this, we simply keep track of the phase retardation along different rays through the aperture, then take its Fourier transform to obtain the amplitude at the focal plane. This approach uses the MTF previously mentioned. For turbulent flows, only homogeneous turbulence was analyzed until recently.[9]

A third technique, wave optics, which is computer intensive, was developed during the 1970s for high-power gas lasers. In it, a wave is propagated from plane to plane along the optical path. A new complex amplitude including aberrations is calculated at each plane and propagated to the next plane. A code applying this technique to aero-optics was developed by Clark.[10]

Because of its accuracy and ease of application, we adopted the use of physical optics for aero-optical predictions, which directly predicts tilt, focus errors, and the blur circle. The boresight error is obtained from the mean tip or tilt of the optical path difference (OPD), or more accurately, from the centroid of the angular location of the blur circle.

Calculational Procedure

The aero-optics procedural steps, from flowfield generation to kill probability determination, are sequentially diagrammed in Fig. 1. The fluid mechanics and aero-optics steps are described here.

Computational Aerodynamics

The aerodynamic computer code FDNS[11] (finite difference Navier-Stokes) was adopted for this study. This code is a pressure-based, nonstaggered grid, chemically reacting, Navier-Stokes solver. An adaptive upwinding differencing scheme is employed for the spatial discretization. The code has equilibrium and finite rate algorithms for computing mixture species concentrations, and thermodynamic, transport, and optical properties.

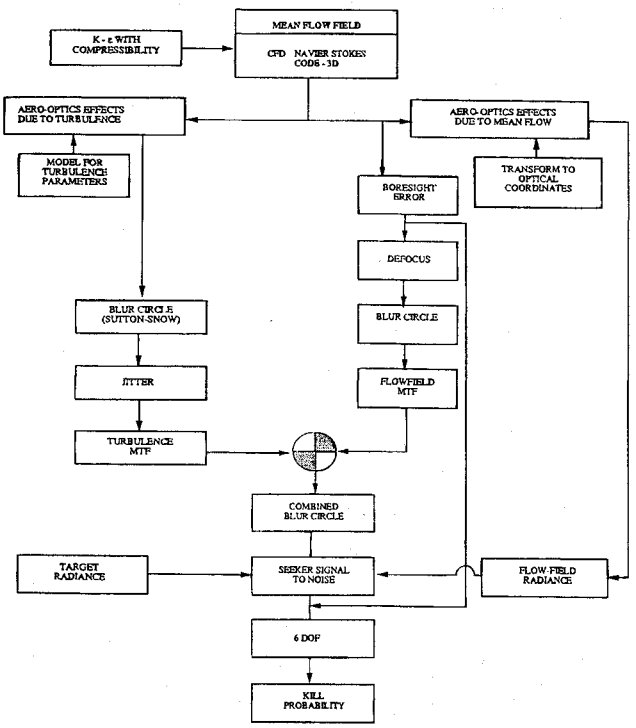

Fig. 1 Aero-optics procedure.

In general, a noniterative time-marching scheme was used; however, subiterations can be used if necessary. To provide smooth shock solutions, adaptive dissipation terms were added to the pressure correction equation. Once the pressure correction equation is satisfied, the velocity field is then updated, and the density field is updated through the equation of state. To ensure that the updated velocity, density, and pressure fields satisfy the continuity equations, the pressure correction solution procedure is repeated several times before marching to the next time step, thereby representing a multicorrector solution procedure.

The turbulent eddy viscosity is employed to model the turbulent regions of flow. A two-equation κ-ϵ model was employed to determine the eddy viscosity component of the effective viscosity. As pointed out by several researchers,[12-14] the standard κ-ϵ model fails to predict the observed decrease in spreading rate for the compressible free shear layers. Concentrating on the κ-ϵ model, the dissipation of the kinetic energy in compressible turbulence was argued to be augmented. Sarkar[12] and Zeman[13] proposed that the total dissipation should be a function of turbulence Mach number M_t, defined by $M_t^2 = \kappa/a^2$, where a is the local speed of sound. In the present study, a compressibility correction term, $E_k = \alpha_1 M_t^2 \bar{\rho}\epsilon$ ($\alpha_1 = 1.0$), has been added to the turbulent kinetic energy equation. Both Sarkar and Zeman postulated that the transport equation for ϵ is unaffected by compressibility. However, the approach taken by Rubesin[15] takes exception to this argument, and he has proposed a correction term for compressibility effects in the ϵ transport equation. We adopted the approach taken by Sarkar and Zeman because it produced the correct spreading when compared to Schlieren photographs.

The parameters for the turbulence aero-optics are derived from the computational fluid dynamics (CFD) results. There are several approaches to accomplish this including equations for the density or index-of-refraction fluctuation[16] or from some other combination of the κ-ϵ equations. We have chosen a simpler method to obtain the turbulence parameter from the mean (time-averaged) flow. Under the assumption of equilib-

rium turbulence, the characteristic length scale of the correlation function of the index-of-refraction fluctuation is given by

$$\ell' = \kappa^{3/2}/\epsilon \tag{1}$$

The fluctuation of the index of refraction is found by first calculating the spatial distribution of the mean index of refraction from

$$n - 1 = \Sigma\, \beta_i \rho_i(x, y, z) \tag{2}$$

where β_i is the Gladstone-Dale constant for the ith species and ρ_i is its spatial distribution. The fluctuation of the index of refraction n' is the product of ℓ' and the local gradient of n using a coefficient of 0.424.

The results of the CFD computation for a sphere-tetracone at zero angle of attack with helium coolant from a slot in front of the window are shown in Fig. 2. The nose radius is 2.413 cm; the window angle is 20 deg; and the coolant inlet height is 0.298 cm. The freestream conditions are $M_\infty = 9.3$, $T_\infty = 233.3$ K, $\rho_\infty = 0.04638$ kg/m^3. Initially at room temperature, the helium flow is at Mach 2 and the static pressure of the helium after expansion is matched to the static shock-layer

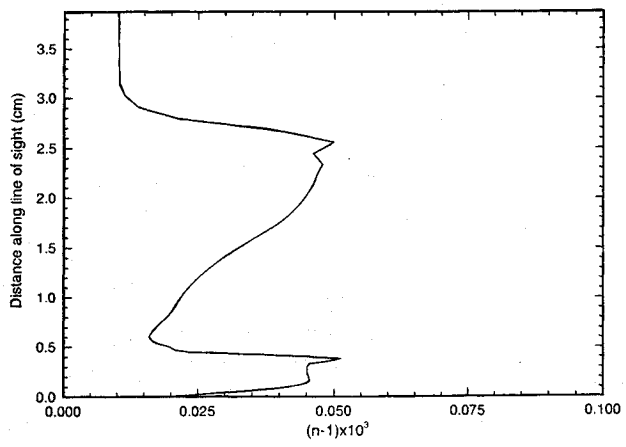

Fig. 2a Mean index of refraction for helium coolant.

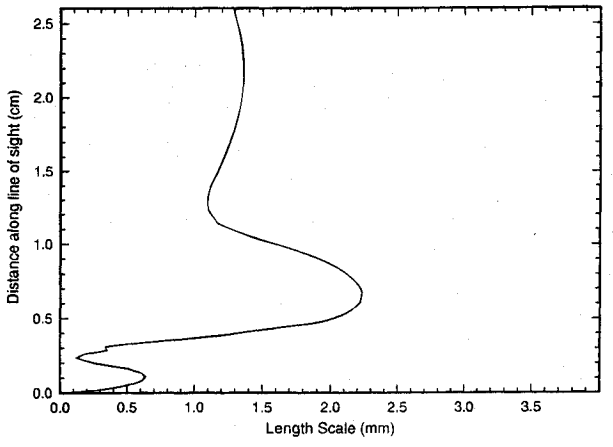

Fig. 2b Length scale of index-of-refraction fluctuation for helium coolant.

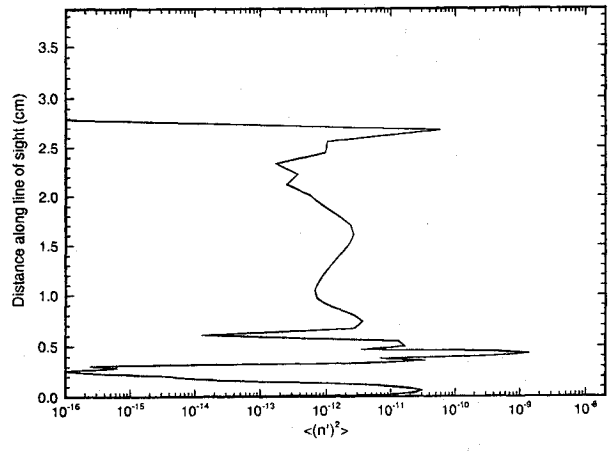

Fig. 2c Variance of index-of-refraction fluctuation for helium coolant.

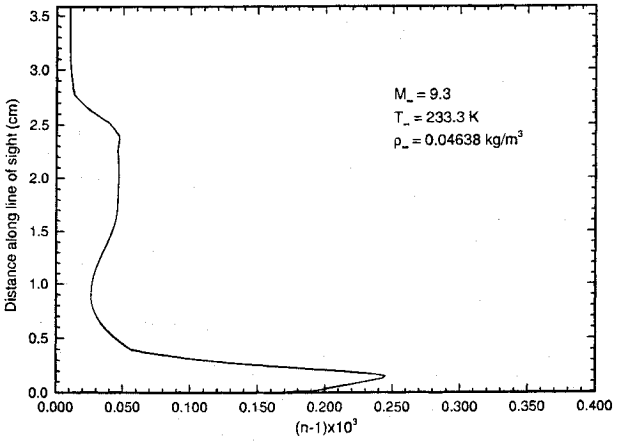

Fig. 3a Mean index of refraction for nitrogen coolant.

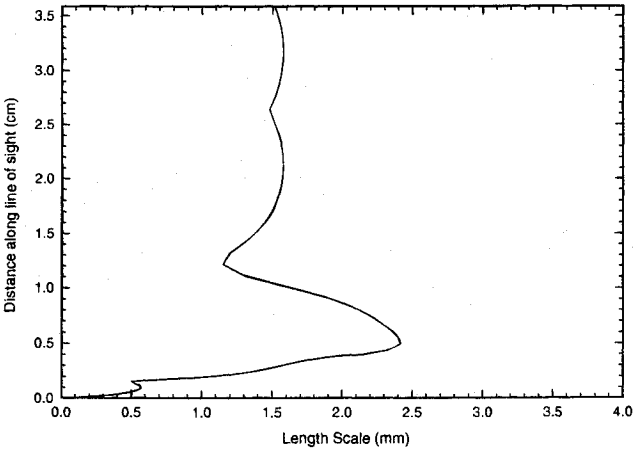

Fig. 3b Length scale of index-of-refraction fluctuation for nitrogen coolant.

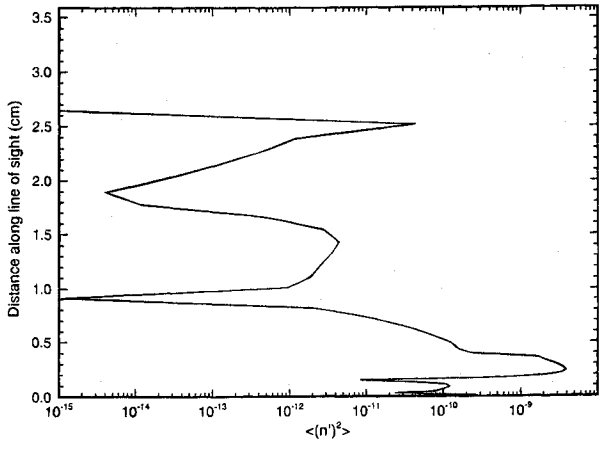

Fig. 3c Variance of index-of-refraction fluctuation for nitrogen coolant.

pressure over the window. Profiles along the chief ray from the center of the window view angle of 20 deg relative to the centerline of the body are shown in Fig. 2. Figure 2a shows the profile of the mean index of refraction. The region beyond 3 cm is the freestream. The bow shock shown is captured in a region where the grid is somewhat coarse, resulting in the smeared index-of-refraction distribution. The density of the outer part of the shock layer that has passed through the oblique shock is 4.73 times greater than the freestream. Progressing toward the surface, the ray encounters the portion of the shock layer that was heated by the blunt nose; hence, the density decreases. At the mixing layer, the index of refraction increases to that of the helium, which is cold due to expansion to $M = 2$ from a room temperature reservoir. The helium is dense because its pressure must match the shock-layer pressure. Adjacent to the window, the index of refraction decreases because the window material is at the helium recovery temperature, warmer than the helium static temperature. Note that if the cone had a sharper nose, the index of refraction would be a closer match to the helium, which would decrease the optical aberrations caused by turbulence.

Figure 2b shows the scale size of the turbulence derived from the κ-ϵ results [Eq. (1)]. Its peak value in the mixing region of about 2mm is smaller than the 5mm thickness of the mixing region, as expected. Figure 2c shows the profile of the variance of the fluctuations of the index of refraction $<n'^2>$. Note that there are fluctuations in the boundary layer near the window, which decrease drastically in the inviscid flow, then increase again in the helium–air turbulent mixing layer. Figure 3 shows the profiles for nitrogen coolant. The large difference in index of refraction between the nitrogen coolant layer and the shock-heated air will cause large density fluctuations. Also, the κ-ϵ method generates turbulent properties wherever there is a velocity gradient, including the shock-heated air. The amount is inconsequential for the present calculations, but the turbulence can be turned off at the outer boundary of the shear layer. In the experiment, measurements of the fluctuation intensity and scale size were not made, hence the experimental validation of the technique is made for σ, which was measured.

Aero-Optics

The aero-optics quantities, both measured and calculated, are the boresight error, wavefront distortion, focal plane intensity distribution, Strehl ratio, and encircled energy. The general assumption is that the mean flowfield produces time-averaged boresight error and blurring, whereas the turbulence produces jitter, scattering, and blurring.

Mean Flowfield Aero-Optic Effects

The starting point is the scalar electromagnetic wave equation for the electric field u

$$c^2 \nabla^2 u = \partial^2 u / \partial t^2 \tag{3}$$

For monochromatic light of wavelength λ, Eq. (3) has an exact solution that connects the electric field at any point a distance r from another point:

$$u(r) = \frac{-iu_o e^{ikr}}{\lambda r} \tag{4}$$

The equation above is known as the Huygens construction. There also is usually a cosine coefficient to account for the angle of the electric field vector and the direction of propagation; it is essentially unity for optical imaging. The use of Eq. (4) is different from the usual perturbation solution of Eq. (3), which leads to the so-called Born approximation. That approximation does not conserve energy and is less accurate.

If u_o is at a point above the disturbed air layer, and is integrated over an area corresponding to the aperture area, we obtain the Huygens-Fresnel law. Expansion of the exponential into Cartesian coordinates yields a constant term, which has zero contribution; a linear term (so-called Fraunhoffer term); a quadratic term (so-called Fresnel term), and so forth. At a focal point, the Fresnel term is of second order and is negligible.

As the rays penetrate the disturbed air, they pick up a optical path difference (OPD) σ:

$$\sigma = \int_0^L (n - 1)\, dz \tag{5}$$

where n is the index of refraction of the medium, in this case air and coolant. This manifests itself as a phase error $k\sigma$, which is added to the exponential of Eq. (4).

To calculate the optical effects of the three-dimensional mean flowfield, optical path differences were computed by passing rays through the CFD grid. As an initially plane wave propagates through a mean flowfield of varying refractive index, the wavefront becomes distorted and tilted. The wavefront tilt is manifested at the focal plane as a lateral displacement of the blurred image pattern.

The CFD calculations described above provide the values of the mean flow properties from past the bow shock wave down the line of sight to the aero-optic window. These properties are known at the nodes (x, y, z) of the CFD grid, which also define the cells between the grid points. Using the mean density field and species concentrations to find the mean index of refraction, the OPD is found by projecting a bundle of rays from the aperture, usually circular, through the CFD grid. A plane coincident with the incoming wave is defined at a position in the freestream where no disturbance to the mean flow is expected. The bundle of rays is then projected parallel to the line of sight through the shock wave, shock layer, shear layer, and boundary layer over the window. Integrating the index of refraction along each ray defines the OPD as follows:

$$OPD(x, y) = \int_0^L \sum_i \rho_i(x, y, z)\beta_i\, dz \tag{6}$$

where β_i is the Gladstone-Dale constant for the ith species. The process is carried out by passing each ray through the cells defined by the CFD grid points. First, the value of the mean index of refraction is found on the face where the ray pierces into the cell by using the following interpolation formula:

$$n = \tfrac{1}{4}[(1 - \epsilon)(1 - \eta)n_i + (1 + \epsilon)(1 - \eta)n_j + (1 + \epsilon)(1 + \eta)n_m + (1 - \epsilon)(1 + \eta)n_k] \tag{7}$$

This expression linearly interpolates over the quadrilateral with $n_i - n_k$, the index of refraction at the nodes and η, ϵ, the intrinsic coordinates found from an iterative solution of a nonlinear equation once the Cartesian coordinates of the pierce point are known. Integration through the cell is carried out using the trapezoidal rule. No contribution to the OPD is taken past the outer surface of the window. The next step was to determine the mean value of the OPD, and subtract this because it has no effect. By using the expression $bx + dy$, the tip d and tilt b are found by minimizing the rms error between the OPD and $bx + dy$. Similarly, the mean focus $f(x^2 + y^2)$ is removed. The calculated optical path differences along a packet of rays from the aperture are shown in Fig. 4 for helium coolant, and the mean tilt is 17.37 μr. Figure 4b shows the OPD after tilt removal. Note that they appear to be nearly concentric circles, indicating a change in focus. In our calculations, we correct for focus, which most telescopes are capable of performing. The residual OPD is shown in Fig. 4c.

With boresight and focus errors removed, the amplitude is found from Eq. (4):

$$u(\Theta_x, \Theta_y) = (4/\pi D^2) \int_{-D/2}^{+D/2} \int_{-\sqrt{(D/2)^2 - x^2}}^{\sqrt{(D/2)^2 - x^2}} dy\, dx e^{-ik\sigma'(x,y)} e^{ik(\Theta_x x + \Theta_y y)} \tag{8}$$

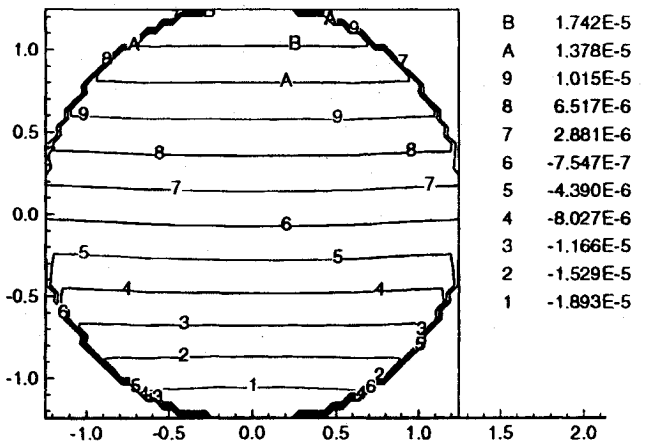

a) After correction for mean value

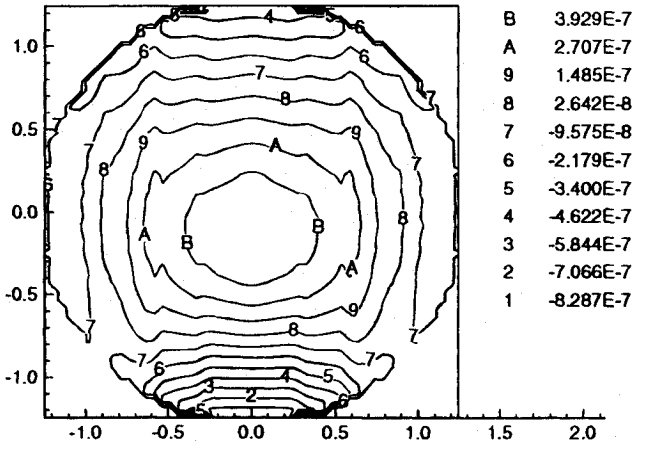

b) After subtraction of tilt (boresight error)

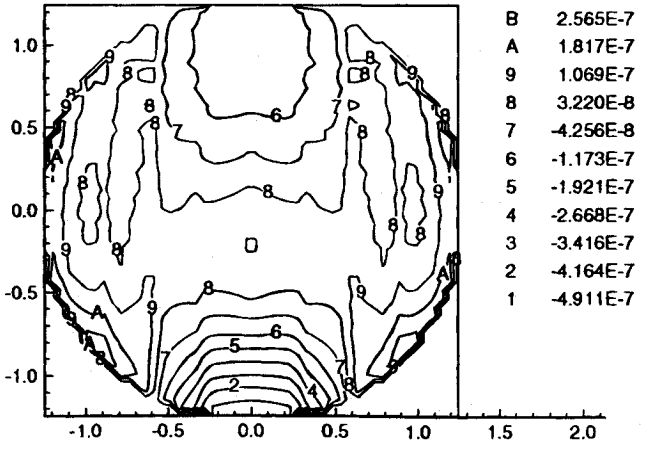

c) For best focus

Fig. 4 Mean flowfield optical path differences in cm (AOEC 3D tare model, 0.633 μ, aperture diam = 2.54 cm).

where $\sigma'(x, y)$ is the OPD with boresight and focusing errors removed. Equation (8) is a two-dimensional Fourier transform of the exponentiated phase error at the focal plane measured from the center of the aperture optical element. The intensity field for the mean flowfield only is obtained by taking the square of the electric field as follows:

$$I(\Theta_x, \Theta_y) = |u(\Theta_x, \Theta_y)|^2 \tag{9}$$

The above is the Sutton-Pond code. Equation (9) was normalized so that for a diffraction limited beam,

$$I(0, 0) = 1.0 \tag{10}$$

The resulting point-spread function, which is the image of a point source, is shown in Fig. 5 as the focal plane intensity distribution along the x axis. Slight increases in the intensity of the second lobe can be seen. For this case, the intensity pattern has a Strehl ratio of 0.99. The Fourier transform of this point-spread function gives the MTF for the mean flow, to be convolved with the MTF of the turbulence, considered next. The product of the mean flow and aperture MTF is given by

$$\tau_{FF}(\xi, \eta)\tau_A(\xi, \eta) = [32I_O]^{-1}k^2D^2 \int_{-\infty}^{\infty}\int_{-\infty}^{\infty} I_{FF}(\Theta_x, \Theta_y)e^{-ik(\Theta_x\xi + \Theta_y\eta)}d\Theta_x d\Theta_y \tag{11}$$

where ξ, η are the Fourier coordinates, I_o is the diffraction-limited central intensity (usually set to unity), D is the aperture diameter, and Θ_x, Θ_y are the angles to the focal plane.

The MTF along the ξ axis derived from the blur circle is shown in Fig. 6. In this calculation, the normalization is to $\pi/2$ instead of unity as a convenience. The curve does not quite reach that value, because the integration indicated by Eq. (11) was not extended to infinity.

Turbulence Aero-Optics Effects

We describe next the image blurring caused by the turbulence. The turbulence randomly perturbs the wave before it encounters

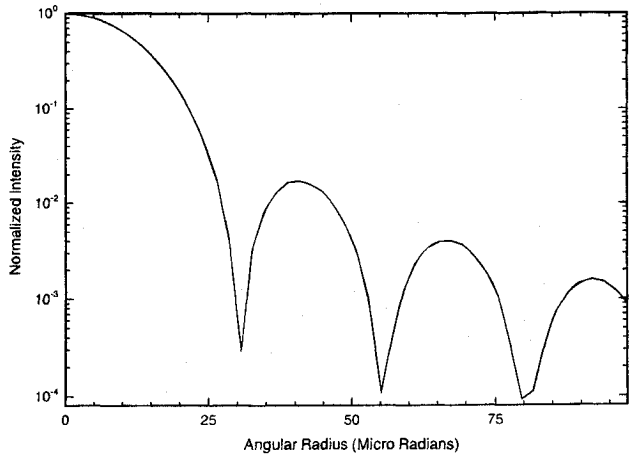

Fig. 5 Mean flowfield intensity vs angle (blur circle for AOEC three-dimensional tare model, 0.633 μ, aperture diam = 2.54 cm).

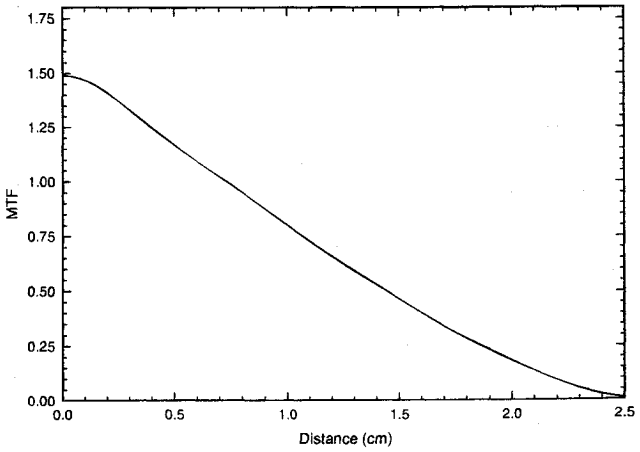

Fig. 6 Mean flowfield modulation transfer function.

an aperture that focuses the beam onto the focal plane. In the absence of disturbances, the focal plane intensity distribution is the well-known Airy disk, the diffraction pattern of an unperturbed plane wave focused by a circular aperture. If turbulence is present, the Airy intensity pattern is reduced, and there is large angle scattering caused by the eddies. The Strehl ratio is defined as the intensity of the turbulence-blurred pattern at its central peak divided by the diffraction-limited pattern at its central peak. The encircled energy (or power) is denoted by the radius in the focal plane that encloses a given percentage of the total incident power. For example, 83% of the incident power is contained in the central lobe of the diffraction-limited intensity.

To obtain the intensity pattern in the presence of turbulence, Eq. (8) is squared and the ensemble average is taken. With a shift in coordinates $\xi = x - x'$, $\eta = y - y'$, the result is a Fourier transform of the turbulence MTF, τ_T given by

$$\tau_T = \exp\left\{-2k^2 \int_0^L \langle n'^2\rangle(z) \times \left[\ell'(z) - \int_0^\infty C(\sqrt{(D^2\rho^2 + \zeta^2)})d\zeta\right]dz\right\} \quad (12)$$

where $\rho = D^{-1}\sqrt{(\xi^2 + \eta^2)}$ and ζ, z are in the propagation direction. For an exponential correlation function, the inner integral becomes $\rho\kappa$, (ρ/ℓ') where κ, is the modified Bessel function of order 1.

Equation (12) is the essence of the Sutton-Snow code. The turbulence-blurred image pattern depends on the propagation path length L through the turbulent layer, the variance (mean square) of the refractive index fluctuation $< n'^2>$, the correlation length of the refractive index fluctuation ℓ', and the associated correlation function C. For shear layers, an exponential correlation function of the refractive index fluctuation is physically realistic.[17] The turbulence length scale ℓ' is the spatial integral of the index-of-refraction correlation function. This approximately represents the separation for which the turbulent motion at two points is uncorrelated; e.g., ℓ' is the size of a turbulent eddy. Another quantity is the rms optical path difference

$$\sigma_{rms} = \left(2\int_0^L \langle n'^2\rangle \ell' dz\right)^{1/2} \quad (13)$$

The turbulence MTF, for the turbulence parameter profiles shown in Figs. 2 and 3, are shown in Fig. 7 for freestream conditions $M_\infty = 9.3$, $T_\infty = 233.3$ K, $\rho_\infty = 0.04638$ kg/m^3.

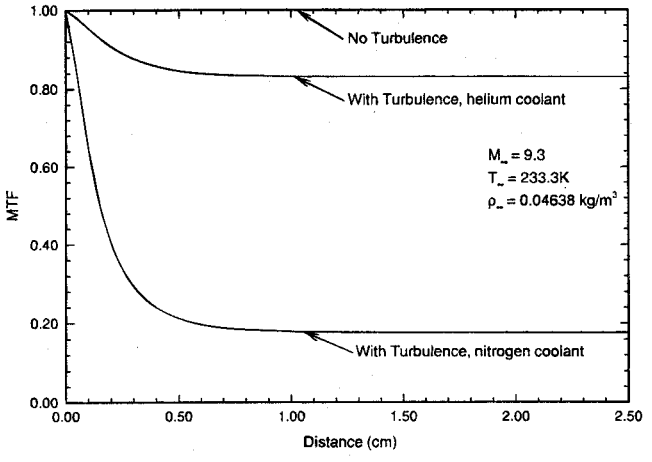

Fig. 7 Turbulence modulation transfer function for helium and nitrogen coolant.

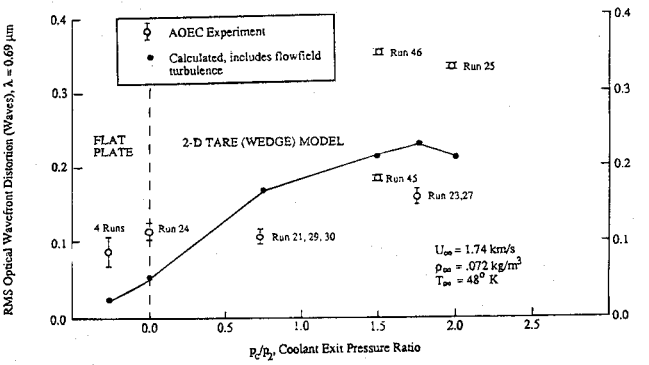

Fig. 8 Comparison between calculated and measured wavefront distortion for nitrogen coolant.

Aero-Optics Sample Results

The Sutton-Snow optical code was validated by comparison with experimental data obtained at the Aero-Optics Evaluation Center (AOEC) of the Calspan/ University of Buffalo Research Center (CUBRC). A two-dimensional blunted wedge tare model was used to provide the basic aerothermal and aero-optic test data. Cases without coolant as well as cases with nitrogen and/ or helium coolant were calculated. We first validated the CFD results by comparison with the measured AOEC flow parameters. The calculated pressures and heating rates were found to be in excellent agreement with the measurements. With confidence that the CFD model was accurately predicting the flow parameters, we proceeded to make comparisons between measured and calculated aero-optics parameters.

Figure 10 shows the comparison between measured[18] and calculated values of rms wavefront distortion, for a flat-plate geometry and a two-dimensional blunted wedge model with coolant (nitrogen) and noncoolant cases. The wavefront distortion data, for each run condition, consist of an interferometric fringe pattern, obtained from holography using a laser beam of 0.69 μm wavelength. The exposure time was 10 μs, much smaller than a turbulence flow time; therefore, no turbulence averaging occurred. The fringe pattern depicts the phase fluctuations produced by the turbulent flowfield. The rms wavefront distortion is deduced from measurements of the deviation of the phase from its mean value, over a diameter of 4.6 cm.

In Fig. 8 the calculated curve matches the trend of the measurements very well, but lies outside the error bars. The major source of scatter is caused by the statistics of σ_{rms}. As a result, a single snapshot interferogram for each run condition does not provide an adequate measure of σ_{rms}. Instead, a number of snapshots is necessary for each condition, which would yield an average value of σ_{rms} and an uncertainty range given by the standard deviation. The measured single interferogram uncertainty range is a standard deviation of 20%,[19] which would account for the scatter of the data points within the trend.

Using the calculated aero-optics turbulence parameters, Fig. 9 shows the intensity and encircled energy for the turbulence-blurred conditions in comparison to diffraction limited for the three-dimensional tare model and helium coolant. The wavelength is 0.633 μm, and the beam diameter is 2.54 cm. The Strehl ratio is 0.83 for this case, demonstrating very small optical loss with helium coolant for this flight condition. Higher Mach numbers and freestream density will increase the optical loss.

Combined Aero-Optic Effects

The Sutton-Pond code performs the complete computation of the blur-circle intensity distribution using the modulation transfer function formulation. The MTFs for the three contributors to the blur are aperture, turbulent flow, and mean flow. The total intensity distribution was obtained by convolving the turbulence effects with the mean flow and aperture effects

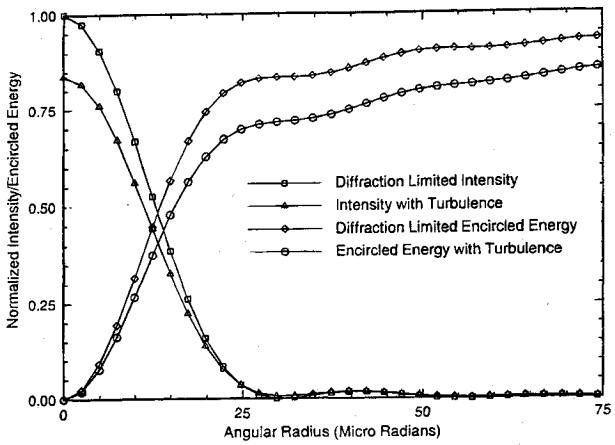

Fig. 9 Calculated angular distribution of focal plane intensity and encircled energy, helium coolant.

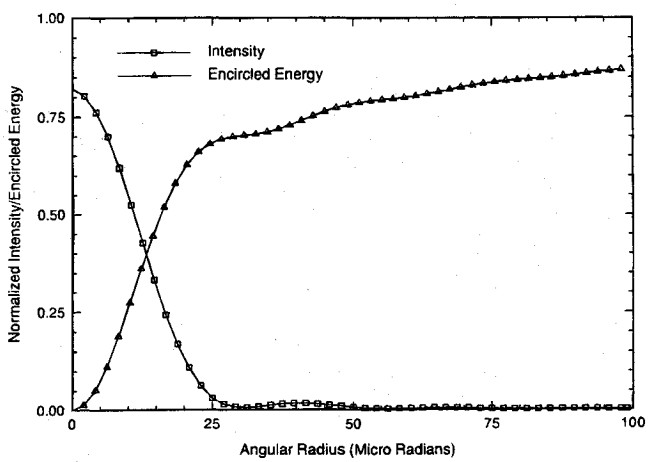

Fig. 10 Combined blur circle for mean flow and turbulence, helium coolant, (AOEC three-dimensional tare model, 0.633 μ, aperture diam = 2.54 cm).

through the inverse Fourier transform of the product of the three individual MTFs:

$$I(\Theta_x, \Theta_y) = 8I_o D^{-2}\pi^{-2} \cdot \int\int_A \tau_A \tau_{FF} \tau_T e^{ik(\Theta_x \xi + \Theta_y \eta)}\, d\xi\, d\eta \tag{14}$$

The Fourier transform of the product results in the intensity and encircled energy distributions shown in Figs. 10 and 11 for helium and nitrogen coolant, respectively. While the helium coolant resulted in a Strehl ratio of 0.83, the use of nitrogen coolant resulted in a far greater loss of a Strehl ratio of 0.17. This effect is consistent with observations.[18] Note that for infrared wavelengths, both coolants would result in practically no loss; but for ultraviolet wavelengths, the loss would be considerably greater. Also, the intensity level on the focal plane of the turbulence scattered light is very low and would generally be useless for centroid tracking at low sensor signal-to-noise ratios. At high signal-to-noise ratios, the turbulence scattered energy will lead to contrast loss of extended images. Note that in order for the MTFs to be multiplied together, they must be uncorrelated, which is valid for this study.

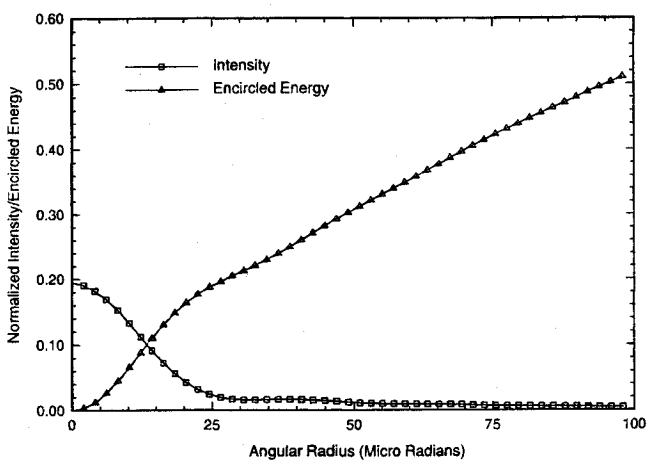

Fig. 11 Combined blur circle for mean flow and turbulence, nitrogen coolant.

The preceding calculations were based on uniform turbulence properties over the aperture (x, y) but which varied in the propagation direction. The effect of nonuniform turbulence has also been investigated.[9] In that work, σ_{rms} increased by a factor of 5.5 in the flow direction x. It was found that there was very little difference (<10%) in the results as compared to assuming uniform turbulence in the chief ray. Therefore, the techniques described in this paper are generally valid.

Discussion

The results we have presented are for an isotropic correlation function and a long exposure. However, it is well known that the correlation function is anisotropic with the scale size in the flow direction about twice that of the transverse distances. This improvement can easily be incorporated.[3] In addition, there is now strong evidence that, in shear and boundary layers, the major axis of the anisotropic correlation function is tilted relative to the flow direction. This can be easily accommodated by a rotation of axis of the correlation function.

For short exposures, Clark has shown that the point spread function psf intensity pattern is broken up in strong turbulence.[10] These random psfs should be used if the exposure time is much shorter than the flow time relative to the turbulence scale length.

Conclusions

This paper has described the hypersonic aero-optics performance predictions. Specifically, a robust three-dimensional Navier-Stokes hypersonic flow code with a compressible κ–ϵ turbulence model has been demonstrated, and three-dimensional optical-to-fluid coordinate conversion has been achieved. In addition, a mean flow aero-optics code for blur circle and boresight error has been developed and demonstrated, and the Sutton-Snow turbulence aero-optics code has been refined and made operational and validated by experimental data. Moreover, mean flowfield and turbulence effects have been combined and demonstrated for the first time. In summary, a robust computational tool for aero-optics effects on signal-to-noise ratio and boresight error has been developed and made operational.

Acknowledgments

The authors thank the sponsors of this work, the BMDO and the USASSDC. In particular, the direction and support provided by Mick Blackledge, Michael Cantrell, Gregory Jones, Michael Huhlein, and Billy Walker is gratefully acknowledged.

References

[1] Liepmann, H. W., "Deflection and Diffusion of a Light Ray Passing Through a Boundary Layer," Douglas Aircraft Company Rept. SM 14397, 1952.

[2] Hufnagel, R. E., "Random Wavefront Effects," *Photographic Science and Engineering*, Vol. 9, No. 4, 1965, pp. 244–247.

[3] Sutton, G. W., "Optical Imaging Through Aircraft Turbulent Boundary Layers," *Aero-Optical Phenomena*, edited by K. G. Gilbert and L. J. Otten, AIAA, New York, 1982, pp. 15–39.

[4] Stein, H. A., and Winovitch, W., "Light Diffusion Through Aircraft Turbulent Boundary Layers," NACA RM A56B21, May 25, 1956.

[5] Booker, H. G., and Gordon, W. E., "A Theory of Radio Scattering in the Ionosphere," *Proceedings of the IRE*, Vol. 38, No. 4, 1950, pp. 401–412.

[6] Sutton, G. W., "Effect of Turbulent Fluctuations in an Optically Active Fluid Medium," *AIAA Journal*, Vol. 7, No. 9, 1969, pp. 1737–1743.

[7] Sutton, G. W., "Aero-Optical Foundations and Applications," *AIAA Journal*, Vol. 23, No. 10, 1985, pp. 1525–1537.

[8] Swigart, R. J., Shih, W. C. L., Wang, J. H., Snow, R., Trolier, J. W., Leone, S. A., Martellucci, A., and Laganelli, A. L., "Hypersonic Film Cooling Effectiveness and Aero-Optical Effects," AIAA Paper 88-3824, 1988.

[9] Sutton, G. W., "The Effect of Inhomogeneous Turbulence on Imaging Through Turbulent Layers." *Applied Optics* (accepted for publication).

[10] Kathman, A. D., Brooks, L. C., Kalin, D. A., and Clark, R. L., "A Time-Integrated Image Model for Aero-Optic Analysis," AIAA Paper 92-2793, 1992.

[11] Wang, T., and Chen, Y. S., "A Unified Navier-Stokes Flowfield and Performance Analysis of Liquid Rocket Engines," AIAA Paper 90-2994, 1990.

[12] Sarkar, S., Erlebacher, G., Hussaini, M. Y., and Kreiss, H. O., "The Analysis and Modeling of Dilatational Terms in Compressible Turbulence," Inst. for Computer Applications in Science and Engineering, ICASE Rept. 89-79, Hampton, VA, Dec. 1989.

[13] Zeman, O., "Dilatational Dissipation: The Concept and Application in Modeling Compressible Mixing Layer," *Physics of Fluids A: Fluid Dynamics*, Vol. 2, No. 2, 1990, pp. 178–188.

[14] Viegas, J. R., and Rubesin, M. W.,"A Comparative Study of Several Compressibility Corrections to Turbulence Models Applied to High Speed Shear Layers," AIAA Paper 91-1783, 1991.

[15] Rubesin, M. W., "Extra Compressibility Terms for Favre-Averaged Two-Equation Models of Inhomogenerous Turbulent Flows," NASA CR- 177556, June 1990.

[16] Smith, R. R., Truman, C. R., and Masson, B. S., "Prediction of Optical Phase Degradation Using a Turbulent Transport Equation for the Variance of Index-of-Refraction Fluctuations," AIAA Paper 90-0250, 1990.

[17] Rose, W. C., and Cooley, J. C., "SOFIA Wind Tunnel Data Analysis and Implications for the Full-Scale SOFIA Aircraft," Rose Engineering and Research, Inc., Incline Village, NV, Oct. 1990, Fig. 23.

[18] Holden, M., Craig, J., and Ratliff, A., "Aero-Optical Facility and Results," *Proceedings of the AIAA Missile Sciences Conference*, Monterey, CA, DTIC, Feb. 1993.

[19] Sutton G., Klein, H., Malley, M., Yu, J., Sapp, O., and Shough, D., "Experimental Measurements of the Optical Path Difference of a Four-Meter Dual Aerocurtain," *Proceedings of the Society of Photo-Optical Instrumentation Engineers*, Vol. 1221, Jan. 1990, pp. 404–413.